Journal of The
Electrochemical Society

Membrane Creep Caused by Porous Transport Layer Compression in PEM Water Electrolysis and the Impact on Hydrogen Permeation

To cite this article: A. Hintzen *et al* 2025 *J. Electrochem. Soc.* **172** 044512

Journal of The Electrochemical Society, 2025 **172** 044512

Membrane Creep Caused by Porous Transport Layer Compression in PEM Water Electrolysis and the Impact on Hydrogen Permeation

A. Hintzen,[z] M. Stähler, and I. Friedrich

Forschungszentrum Juelich GmbH, Institute of Energy and Climate Research, IET-4: Electrochemical Process Engineering, 52425 Juelich, Germany

Reducing hydrogen crossover is important for safe operation of polymer electrolyte membrane (PEM) water electrolyzers. The influence of catalyst coated membrane (CCM) properties, operating conditions, and cell assembly on hydrogen crossover have already been investigated. Recent investigations show strong pressure gradients in test cells used. Additionally, mechanical analysis shows membrane creeping under comparable pressure conditions. These findings raise the question whether the membrane creep during cell operation has an impact on hydrogen crossover. The present study addresses this question and presents results that show correlations between contact pressure, membrane creeping, and hydrogen crossover. CCMs were installed in a commonly used test cell with different contact pressure conditions. Because membrane creeping depends on its swelling state, some of the CCMs were installed wet. The influence of the different assembly modes on cell performance, hydrogen permeation, and membrane creeping were investigated. The study shows a strong dependence of the membrane thickness distribution on the installation situation of the CCM after several hours of operation. The contact pressures commonly used in PEM water electrolysis can lead to strong membrane creep during operation of the CCM, independent of electrochemical reactions. The higher the contact pressure, the stronger the membrane creep and the hydrogen crossover.
 [DOI: 10.1149/1945-7111/adcd00]

Manuscript submitted January 9, 2025; revised manuscript received April 10, 2025. Published April 25, 2025.

Supplementary material for this article is available online

Polymer electrolyte membrane (PEM) water electrolysis (WE) in combination with renewable energy sources is a promising technology for producing hydrogen as an energy carrier. The PEM WE technology is particularly suitable for fluctuating and intermittent energy supply and produces hydrogen in high current density ranges with high gas purities, and has a good and fast system response compared to alkaline electrolysis systems.[1–4]

A reduction of ohmic losses is one method to further increase the efficiency of PEM water electrolyzers which can be achieved by lowering the membrane thickness.[5–7] However, a decrease in membrane thickness results in an increase of permeation. Hydrogen permeation through the membrane not only leads to a declining efficiency of PEM WE cells,[6,8] but also poses a safety risk as the formation of explosive gas mixtures becomes possible (lower explosion limit of hydrogen in oxygen ~4 vol%).[9]

A further option to increase the efficiency is to reduce the contact resistances between the CCMs and the porous transport layers (PTLs). This is achieved by increasing the contact pressure, which is adjusted during cell assembly by compressing the PTLs. The higher the compression, the lower the contact resistance. But, Stähler et al. were able to show that the higher the compression of the PTL on the cathode side, the higher the hydrogen permeation rate.[10] It is important to find a good balance in order to achieve a low contact resistance between the electrode and the PTL without applying too much compression, which has a detrimental effect on hydrogen transport.[10–15] Martin et al.[16] expanded the study on PTL compression influencing the hydrogen crossover. They also investigated the contact pressure distribution in more detail by using pressure-sensitive films during cell assembly, at the beginning when the cell starts to be commissioned. This pressure distribution shows a very inhomogeneous distribution over the active area with very low contact pressures around the channel structures of around 1 MPa and up to contact pressures of over 25 MPa at the ribs of the flow field used. Since the analysis is only performed for dry-mounted CCMs, it can only be assumed that the contact pressure increases with operation as the membrane begins to swell when the cell is flushed with water and reached target temperature. The significance of these results is increased by the publication of Al-Baghdadi et al.[17] about a yield strength of the Nafion™ membrane material used, which is expected to be at about 2.3 MPa under the operating conditions applied in the study by Martin et al.[16]

The combination of the applied contact pressure and the yield strength information predicts that the membrane material will creep under the conditions applied in the study of Martin et al., creating thinner but also thicker regions. The thinner regions can be more easily damaged than the thicker ones, especially when thin membranes are used. In addition, it is expected that the thinner areas will lead to higher permeation rates and thus to increased permeation overall.

Up to now, cross-sectional studies of CCMs to investigate changes in membrane thickness are rarely carried out, although only in small sections and with a manageable number of measurement points.[18–21] However, some studies in cross-sectional surveys of CCMs show that there are significantly thinner areas within CCMs that become hotspots for development of pinholes within CCMs. Garbe et al.[22] show that CCMs with Nafion™ 117 creep at elevated cell temperatures during cell operation and even exhibit membrane thickness distribution measured in SEM cross sections at 5 different points in the CCM. A detailed analysis of how the mechanical stress caused by cell assembly affects membrane creep and thus performance and hydrogen permeation has not yet been performed.

The subject of this work is therefore to investigate the membrane creep within the CCM caused by different PTL compression conditions in PEM electrolysis and the impact on hydrogen permeation. For this, different contact pressure conditions in a PEM-WE test cell were realized, a fixed electrochemical test protocol was applied repeatedly to detect the temporal changes and the impact of the pressure conditions on the membrane thickness distributions was investigated after the test by cross-sectional analysis.

The findings clearly show the permanent membrane deformation induced by creep under typical PEM-WE operating conditions and the impact on the change in the membrane thickness distribution and on the hydrogen permeation over time.

[z]E-mail: an.hintzen@fz-juelich.de

Experimental

Catalyst coated membrane preparation.—By using the decal method, the CCMs were fabricated, as described in a previous work.[10,23,24] For the anode production, an iridium-containing dispersion was coated to a 140 μm thick glass fiber reinforced PTFE substrate using a slot die (TSE Troller AG) with a coating width of 200 mm. (CF206, Saint-Gobain) (anode composition: 70 wt% iridium(IV)oxide (Premion™, Alfa Aesar) and 30 wt% Nafion™ ionomer (D1021, Chemours)). The cathode, which consisted of 85 wt% carbon supported platinum catalyst (60% Pt, EC-300J, PK catalyst) and 15 wt% Nafion™ ionomer (D1021, Chemours) was also coated with a TableCoater with a slot die width of 200 mm (TSE Troller AG). The coated substrates were cut into (4.2 × 4.2) cm^2 pieces and hot pressed at 150 °C and 0.025 kN cm^{-2} onto a Nafion™ 212 membrane. The resulting catalyst loading was (1.05 ± 0.05) mg_{Ir} cm^{-2} for the anode and (0.30 ± 0.05) mg_{Pt} cm^{-2} for the cathode. For the wet cell assembling, the CCM was pre-swollen what lead to an increase of the active area to (4.7 × 4.7) cm^2 what resulted in a reduced catalyst loading of about (0.84 ± 0.05) mg_{Ir} cm^{-2} for the anode and (0.24 ± 0.05) mg_{Pt} cm^{-2} for the cathode.

Cell assembly.—The CCMs were electrochemically characterized by using an in–house manufactured test cell. The meander structured flow field on the anode side is platinum plated titanium and gold plated titanium on the cathode side. A (340 ± 2) μm thick titanium felt (Bekipor® Titanium, 2GDL-10-0.35, Bekaert, porosity 68%) iridium sputtered on both sides with dimensions of (4.2 × 4.2) cm^2 is installed as PTL on the anode side. The sputtering was carried out as published by Liu et al.[25] The amount was approximately (0.08 ± 0.02) mg/cm^2. To ensure even pressure distribution, there is an additional (1013 ± 3) μm thick iridium coated titanium felt (Bekipor® Titanium, 2GDL-40-1.0, Bekaert, porosity 56%) between the flow field and the thin titanium PTL.

A carbon nonwoven PTL from Freudenberg (H23I2, (217 ± 2) μm) with dimensions (4.2 × 4.2) cm^2 was used on the cathode side. To investigate the influence of a non-uniform contact pressure distribution, only the thin carbon PTL (C-PTL) was installed between the flow field and the CCM in the "uneven"-case. To achieve a cell structure with a balanced contact pressure distribution a (1026 ± 2) μm thick platinum coated titanium felt was additionally installed between the flow field and the C-PTL in the "even"-case. For the sake of simplicity, we will refer to 1 mm thick PTLs in the case of even contact pressure distribution. The cell was assembled with combinations of PTFE and PI flat gaskets. All gasket thicknesses for the titanium PTLs (Ti-PTL) were chosen to be the same thickness as the Ti-PTL, the flat gaskets of the C-PTL were this way selected resulting in compression values of k_{low} = 22% or k_{high} = 42%. The increase in membrane thickness due to subsequent swelling upon contact with water in the test cell was not considered when adjusting the compression rate.

To reduce the risk of short circuits caused by the sharp edges of the titanium PTLs, an additional 12 μm thin polyimide (PI)-subgasket was installed between the CCM and the PTL on both sides of the cell, resulting in an active area dimension of (40 × 40) mm^2. The details of the cell assembly are shown in Fig. 1.

The CCM was assembled either dry or wet, an overview of the installation variants with the markings used in this study is summarized in Table I. For wet installation the CCM was immersed in Milli-Q® water ($\sigma_{initial}$ = 0.05 μS cm^{-1}), heated to 80 °C for 1 h and then left in Milli-Q® water at room temperature for 18 h overnight. The swollen CCM was then assembled underwater using the same PTLs, gasket thicknesses and bolt tightening torques as for the dry installed CCMs. The test cell was set up with eight tie rods that were gradually tightened to a torque of 10 Nm. It is conceivable that the wet-installed membrane, the dimensions of which are chosen so that it lies between the seals up to the edge of the cell, dries out during operation and changes its thickness. This would have an impact on the cell compression. However, this possibility will not be discussed in more detail below, since an assumed change in the thickness of the membrane of 10% would result in a change in thickness of 5 μm. In view of the mentioned thickness variation of the C-PTL (+/−2 μm), it can be assumed that 95% of the C-PTL thickness is in the range between 213 μm and 221 μm (double standard deviation). In the authors' estimation, such minimal changes in thickness are hardly detectable with a technical laboratory cell.

The cells were assembled according to the instructions described in Fig. 1 and Table I. The two different compression values k_{low} and k_{high} of the C-PTL that were realized by the different gasket thicknesses were either leveled by applying 1 mm thick Ti-PTLs on both sides of the CCM (even) or not (uneven). Under the test conditions mentioned, the compressibility of the Ti-PTL is negligible compared to the C-PTL.

Test protocol and test rig.—After the cell was assembled, it was installed in an in-house test rig and electrochemical measurements were carried out. The test rig setup was already described in previous works.[10,26] The cell was flushed on the anode and cathode side with water preheated to 80 °C (25 g min^{-1}), brought to a cell temperature of 80 °C, and examined for a short circuit in a preliminary measurement. Initial cell voltages below the decomposition voltage of water were applied, a defined protocol was run, and the current density was measured, similar to Stähler et al.[27] An impedance spectrum at 1.45 V was then recorded, using an electrochemical workstation (Zennium Pro, Zahner).

At this point, it should be briefly pointed out that the PEM-WE test cell with an active area of 16 cm^2 in the setup used has an ohmic resistance of about 32 mOhm cm^2 which corresponds to a measured resistance value of 2 mOhm. The total measured resistance value is important to determine the uncertainty to the measured impedance values according to the manufacturer accuracy contour plot of the device. According to this plot, phase errors in the range of 3° and amplitude errors of 2% have to be expected in the range of 500 Hz and 10 kHz, when using the Zennium Pro device. Above 10 kHz the error is larger. The high frequency resistance (HFR), which contains information about the membrane resistance, and which should show the expected changes in the membrane, is therefore strongly influenced by device-related measurement errors. These errors are lower in the Zennium Pro device than in other devices available in this study that allow larger currents. Because the current of the Zennium Pro is limited to 3 A, impedance spectra are only recorded at low current densities (at 1.45 V).

Polarization curves were measured 20 times in succession using the following steps: 1.45 V, 1.50 V, …1.80 V, 1.70 V, …1.50 V, 1.45 V. Each cell voltage was kept constant for 15 min. Finally, a short-circuit measurement was carried out again and the impedance measurement was repeated with the same cell settings. Each measurement was performed automatically, so the total measurement time was the same for each cell. The measurement time was 75 h. During the measurement, the current density, water conductivities at the anode/cathode in- and outlets were measured.

The water-oxygen mixture at the anode outlet was fed into a gas separator and the water in the gas phase was condensed out by a cooler. The dew point in the oxygen at the cooler outlet was 0 °C for all oxygen flow rates measured in this study, checked with a dew point mirror (HX 373, MBW). The hydrogen concentration in the oxygen was then measured by a thermal conductivity sensor (FTC300, Messkonzept GmbH, measurement range 0–3 vol%, carrier gas: oxygen) that was calibrated with hydrogen in oxygen calibration gas (Linde, relative accuracy ±2%) which was passed through the test rig to the sensor. The dew point of this gas mixture was 0 °C. The accuracy of the FTC-sensor according to the calibration is: 0.02·(read value) +0.0001. The details of this setup and the measurement devices used are described in previous work.[10,26,27] The measurement uncertainty (standard deviation) was determined using the measuring instrument uncertainties in

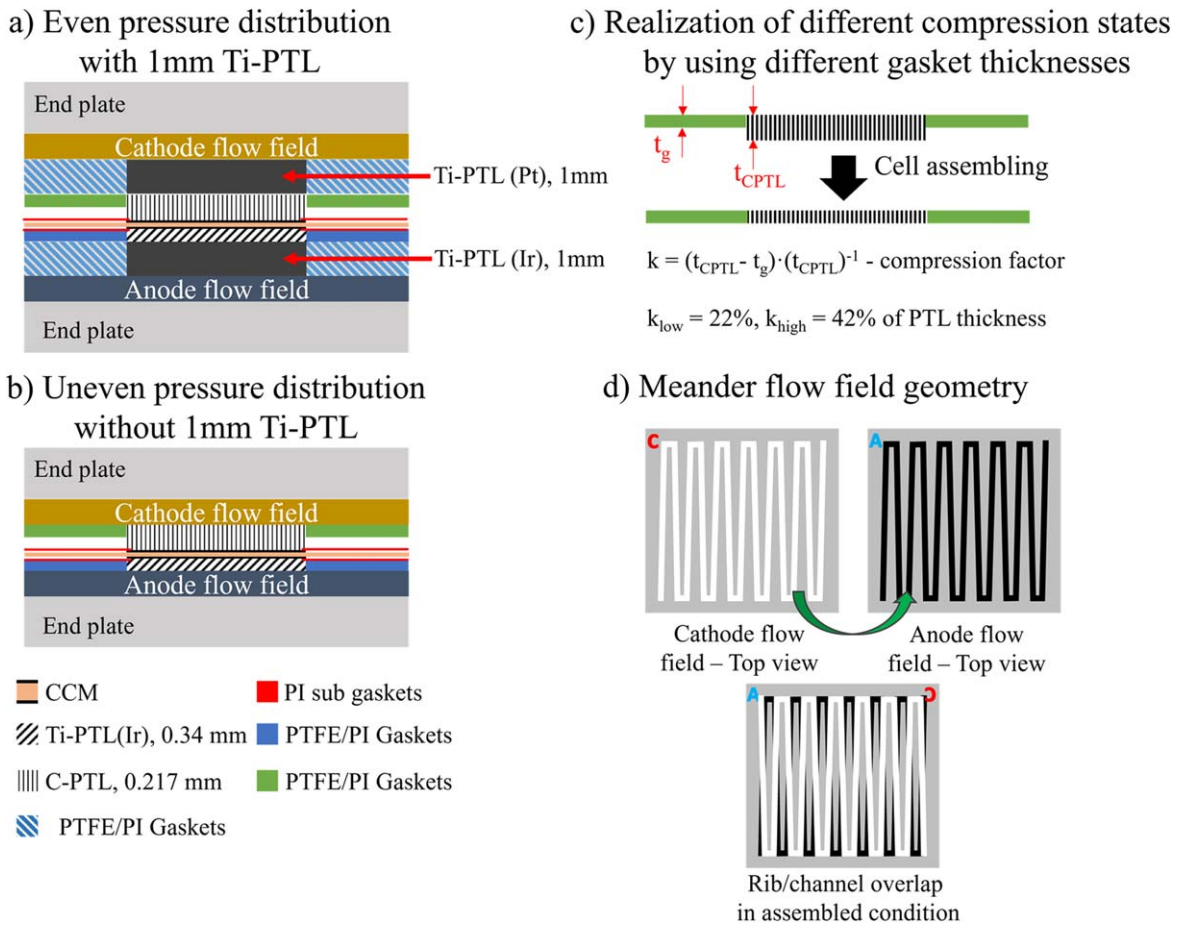

Figure 1. Sketch of the test cell setup. (a) The setup with even pressure distribution, viewed from bottom to top, consists of the following components: The end plate, the platinum-coated titanium anode flow field, a 1 mm thick iridium-coated titanium PTL including a flat gasket of the same thickness, a 340 μm thick iridium-coated Ti-PTL with the accompanying flat gasket of the same thickness, a 12 μm thin PI (polyimide) sub gaskets as membrane protection from the PTL edges, the CCM, followed by the carbon PTL that comes on the cathode side, which was compressed by the compression factor k_{low} or k_{high} by selecting the appropriate flat gasket thickness t_g. To even out the contact pressure, a 1 mm thick titanium PTL, which is coated with platinum, is also installed on the cathode side. Compression of the Ti material is prevented by choosing the same seal thickness. This is followed by the gold-plated titanium flow field and the end plate. (b) The structure with uneven pressure distribution consists of the same components, except for the 1 mm thick Ti-PTLs on the anode and cathode flow field and the associated flat gaskets. (c) Adjustment of the compression factor by choosing an appropriate gasket thickness t_g in relation to the CPTL used with thickness t_{CPTL}. (d) Top view of the anode and cathode flow field geometry used for the experiments with a schematic of the overlapping structure in assembled condition.

Table I. labeling used for the types of cell assemblies investigated in this study.

Marking	CCM assembling	Additional 1 mm Ti-PTL	Compression factor k
k_{low} even-dry	dry	Ti-PTL(Ir) anode, Ti-PTL(Pt) cathode	22%
k_{low} even-wet	wet	Ti-PTL(Ir) anode, Ti-PTL(Pt) cathode	22%
k_{low} uneven-dry	dry	no	22%
k_{low} uneven-wet	wet	no	22%
k_{high} even-dry	dry	Ti-PTL(Ir) anode, Ti-PTL(Pt) cathode	42%
k_{high} even-wet	wet	Ti-PTL(Ir) anode, Ti-PTL(Pt) cathode	42%
k_{high} uneven-dry	dry	no	42%
k_{high} uneven-wet	wet	no	42%

combination with error propagation according to the following procedure:

−Measuring H_2 in O_2 concentration c[10]

$c \pm dc$ with $dc = 0.02\cdot c + 0.0001$

−Measuring oxygen flow rate $V_s(O_2)$; s-standard conditions

$V_s(O_2) + dV_s(O_2)$ with $dV_s(O_2) = 0.004\cdot V_s(O_2) + 0.002$ l_s/min[27]

−Calculating H_2 in O_2 (related to the O_2− cell output)[10]

$c_{cell} = (V_s(O_2)+I\cdot k)/(V_s(O_2)+I\cdot k/c)$

a. I - electrical current
b. $k = Ts\cdot R/(4\cdot F\cdot ps)$

i. Ts—standard temperature (273.15 K)
ii. ps—standard pressure (101325 Pa)
iii. F—Faraday constant

iv. R—general gas constant

−Calculation of measurement uncertainty of ccell via error propagation:

$$dc_{cell} = ((\partial c_{cell}/\partial V_s(O_2)) \cdot dV_s(O_2))^2 + ((\partial c_{cell}/\partial I) \cdot dI)^2 + ((\partial c_{cell}/\partial c) \cdot dc)^2)$$

$$= 1/(V_s(O_2) + I \cdot k/c)^2 \cdot [(1/c^2 \cdot ((I \cdot k \cdot dV_s(O_2))^2 + (dI \cdot k \cdot V_s(O_2))^2)^{0.5} + (I \cdot k \cdot (V + I \cdot k) \cdot dc/c^2)^2]$$

The conductivity of the water in both circuits was kept constant by using ion exchange resins (Amberlite® IRN-150, Supelco®).

Contact pressure investigation.—Before the measurement, the contact pressure distribution over the active area of the test cell was analyzed. The analysis was carried out using pressure-sensitive films from FUJIFILM of the types LLLW, LLW and LW (Prescale™).

Since the flow of force through the cell is affected by each additional component installed and the test cell will also deform when heated to 80 °C, the measurements with the foils, which only allow an operating temperature of up to 35 °C, can only provide approximate values for the pressure values. Additionally, Irmscher has shown that the measurement results differ slightly when the films are used individually compared to when all foils are used simultaneously.[28] There are several options for positioning the measuring foils in the test cell, all of which will produce slightly different results, as each layer of the layer system used can influence the force flow through the cell. Since the focus of the present study is on the question of whether the pressures close to the membrane are large enough to trigger creep processes in the membrane and thereby influence hydrogen permeation, the foils were positioned as close to the CCM as possible. In this study, we decided to position the Prescale™-films between the CCM and the C-PTL. The films were placed so that the most pressure-sensitive one rested on the CCM and then placed in descending order toward the C-PTL. A new C-PTL was used after each assembly and disassembly. By varying the gasket thicknesses and either installing the thick anode and cathode PTLs or not, it was possible to visualize the initial pressure distribution within the cell for even and uneven pressure distribution. The pressure-sensitive films leave a color imprint on a carrier film that is colored more intensely red depending on the pressure level. The three different film types cover a different pressure range. After evaluating each film with the software FPD-8010Win (FUJIFILM), the three resulting images were layered on top of each other and the overall pressure distribution could be displayed. Further processing of the data was then carried out using MATLAB 2023a (The MathWorks, Inc.), which allowed the frequency distributions to be determined.

Cross-sectional analysis.—After the measurement, the cell was slowly cooled down while the water flow was running. When the cell reached room temperature, it was removed from the test stand and dried in the assembled state. Using a vacuum pump, laboratory air at 23 °C and 50% humidity was passed through the cell (ambient conditions) and dried in this way overnight. The cell was then disassembled. In this way, the CCM could not change its width and length after removal, which particularly happens with CCMs that have been removed when wet.

Samples of 12 mm to 16 mm length of each CCM were then embedded in an epoxy resin. Before embedding, the samples were fixed with metal embedding springs on the left and right and the clips were in turn fixed on a double-sided adhesive. Finally, the cured samples were cut and polished. The sample cross section was chosen to be transverse to the course of the flow field in order to obtain a rib/channel/rib sequence and to map the influence on the sample deformation. Images of the cross sections were taken with an optical microscope (Stemi 2000-C with AxioCam ICc3, Zeiss) along the entire length of the sample. The individual images were then stitched together using a graphics program to create a coherent image. Using MATLAB 2023a in combination with the Image Processing Toolbox, the contour of the membrane could be detected and the point between the anode-membrane and membrane-cathode transition could be analyzed across each column of pixels. The distances between the points were determined over the entire sample length and thus the frequency distribution of the membrane thickness over the entire sample length was shown. The scaling was approximately 0.5 μm/pixel, resulting in 24,000–32,000 membrane thickness values per image.

Results and Discussion

Contact pressure investigation.—The visualization of the contact pressure distribution across the active area for the different cell assemblies is visualized in Fig. 2. The pressure sensitive films are not suitable for depicting a continuous pressure curve or for depicting the situation in cell operation under the influence of water swelling and temperature. They merely represent the initial state, i.e. the pressure distribution that acts on the dry CCM when the cell is assembled. This condition is the same for CCMs assembled with the same PTL and seal combination whether installed dry or wet. It is expected that the contact pressure between electrode and PTL will increase more during operation with the dry assembled CCM than with the pre-swollen CCM, since the membrane begins to swell upon contact with water and will press harder against the PTL. The visualization of the even pressure distribution (Figs. 2a–2b) stands out clearly from that of the uneven pressure distribution (Figs. 2c–2d). While the structure of the meander flow field (see Fig. 1d) can only be seen moderately faintly in Figs. 2a, 2b, the structure in Figs. 2c, 2d can be seen very clearly. At low compression values, the meander structure is more clearly visible than at higher compression values, since the pressure transfer from the PTL to the CCM acts further into the channel structure and not just via the ribs when the compression is increased.

The evaluation of the image analysis in MATLAB enables the representation of the frequency distribution of the different pressure levels over the entire active area. Figure 2e shows the frequency distribution for the different cell arrangements. Here it becomes clear how large the areas are that are only exposed to very low contact pressures by using thin PTLs in combination with meander flow fields. Over the channel geometry the contacting of the active area is only in the range of 0.2 MPa–0.75 MPa.

When comparing the same compression value, but with an even or uneven cell assembly, it becomes clear that the pressure prevailing over the entire active cell area in an even assembly is only present in the area of the flow field ribs in the uneven state. With "k_{low} even" approximately 85% of the area is in a pressure range of 0.75 MPa–1.5 MPa, while this pressure range only acts on approximately 35% of the total area at "k_{low} uneven." The situation is similar with the higher compression rate. The relevant pressure is in the range of 1.5 MPa–3 MPa, which acts uniformly on about 90% of the contacted area and only contacts about 40% of the area when the cell is assembled with thin PTLs only. As follows from the work of Al-Baghgdadi,[17] it is to be expected that the membrane begins to creep at pressures greater than approximately 2.3 MPa. Therefore, areas with smaller and thicker membrane thicknesses must be formed in the CCM which can affect the hydrogen permeation. How the different contact pressure modes affect the hydrogen permeation is presented in the next section.

Polarization curves and hydrogen crossover.—It is unknown how much time the expected membrane creep needs during operation. Since a slow creep in membrane material was to be expected during operation, the polarization curves were repeated 20 times to record the progressive development. Each measurement was

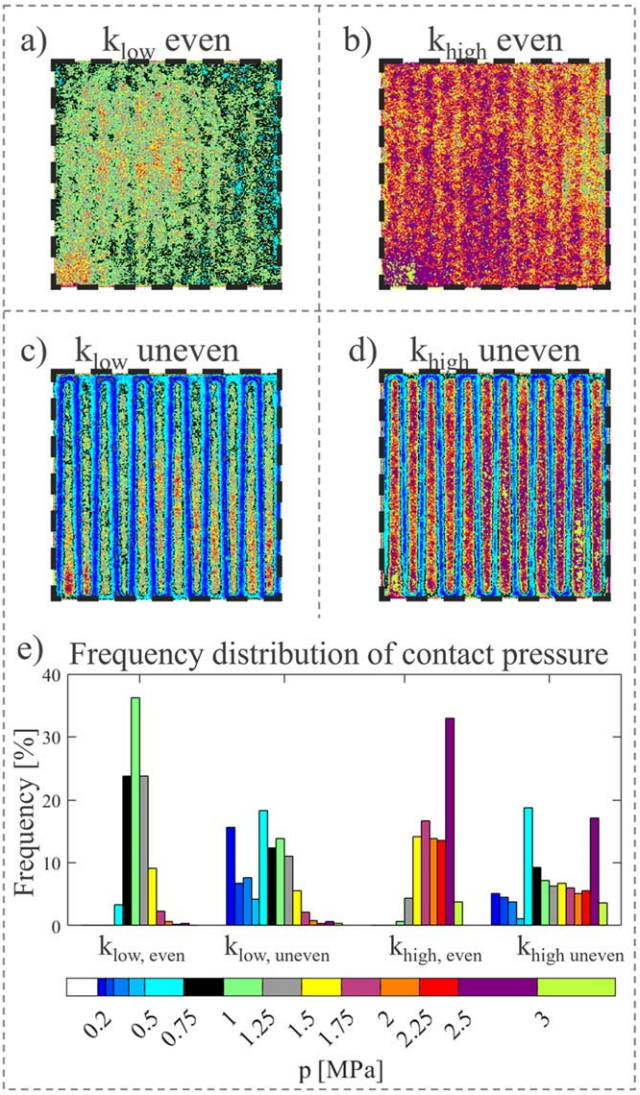

Figure 2. Evaluation of the contact pressure measurement for the 4 different cell assemblies. (a) and (b):Left: k_{low}, right: k_{high} with narrower pressure distribution by using the 1 mm thick Ti-PTLs. (c) and (d): Left side k_{low} and on the right side the high compression value k_{high} with uneven pressure distribution. Here the flow field structure is clearly transferred to the contact pressure distribution on the CCM. As compression increases, the channel structure becomes increasingly narrow. (e) The diagram shows the frequency with which the respective pressure area in the corresponding film was triggered for the different cell structures (Corresponding to the colored pressure bar in the legend). Uneven has a broader distribution of the pressure ranges, since the small pressure ranges are triggered, especially in the channel structures.

carried out automatically so that the measurement times were comparable.

After each cell was put into operation and the first impedance measurements were completed, the polarization curves were run potentiostatically 20 times in a row. The voltage was gradually increased and then slowly reduced again in defined steps. Each voltage was held for 15 min. The results of the first and last polarization curves and the accompanying hydrogen in oxygen concentrations are shown in Fig. 3. Each assembling mode, "k_{low} even," "k_{high} even," "k_{low} uneven," and "k_{high} uneven" is presented separately in Figs. 3a–3d, wet and dry mode together in one chart. Figures 3a–3d also present the evolution of current density and H_2-in-O_2 concentration over the 20 cycles at a cell voltage of 1.8 V.

At this point it should be pointed out that it makes a big difference whether a CCM was installed dry or wet. The dry-installed CCMs experience the applied contact pressure and the additional swelling pressure during operation in comparison to the wet-installed CCM. Furthermore, the membrane thickness distributions in Figs. 6 and 7 demonstrate that local areas can be formed with much thinner and much thicker membrane thicknesses in comparison to the initial membrane thickness. This implies very different local current densities within the active area of the cell depending on its assembly state. In the authors' view, a comparison of the voltage-current density relations, for example in Fig. 3b, is not justified, since Figs. 7a2 and 7b2 clearly shows that the thickness distributions of the membranes are significantly different. This leads to differences in the local current density, although it is still unclear how the interaction of these different areas leads to the measured values. One cannot assume either an equipotential surface or a uniform current density. In addition to the observed membrane deformation the precious metal loading, as described at the beginning, is different due to the pre-swelling of the membrane, which makes a direct comparison of the performance data additionally difficult.

The polarization plots therefore only allow to say that a larger or smaller current flows at a selected voltage of U, without being able to analyse this in more detail electrochemically under the given circumstances. This of course also applies to the H_2-in-O_2 concentration - current density correlation. However, since the permeation is measured outside the cell, it can be determined that more or less hydrogen comes out of the cell while using the same settings for the test cells.

The analyzes regarding the results presented in Figs. 3a–3d are therefore intended to show only to what extent uniform or uneven contact of the active surface with medium or high contact pressure can influence the polarization and the hydrogen cross-permeation.

All diagrams in Figs. 3a–3d show in the left column the cell voltage and hydrogen concentration in the anode gas as a function of current density, while the right column presents the current density and hydrogen concentration at 1.8 V as a function of cycling rate. Considering the current density reached at 1.8 V as a function of cycling rate, a significant increase in performance can be seen for each cell mode from cycle 1 to cycle 20. For each cell mode, a plateau is reached over the cycles, which is achieved faster with higher compression than with lower compression.

Things look a little different with the hydrogen crossover. Looking at the region at higher current densities, which is more interesting for hydrogen production, different developments can be seen over the 20 cycles, depending on whether the cell is assembled with a high or low compressed C-PTL. At the low compression rate, the H_2-in-O_2 concentration on the anode shows an almost constant course of around 0.3 vol% over the 20 cycles. The differences between dry and wet are within two times of the measurement uncertainty (the error bars in Fig. 3 represent the single standard deviation of the measurement). In contrast, at high compression, hydrogen permeation increases significantly from cycle to cycle. The course differs here on the one hand by whether the cell was installed dry or wet and whether the PTL is compressed evenly or unevenly over the active area. The clearest increase can be seen in the cell with the "k_{high} even-wet" assembly, where, in contrast to the polarization curve, no plateau is reached. Permeation increases from cycle to cycle and, most likely, will continue to increase beyond that. These results were confirmed by repeating the measurements. The variations of the measured hydrogen-in-oxygen concentrations were within twice the presented error bars in Figs. 3a–3d.

It is already known from previous work that higher PTL compression leads to an increase in permeation.[10,16] However, the authors of this study have not yet seen any studies showing that a sustained increase in permeation can be observed while repeating the measurements. The starting values in cycle 1 are comparable for all installation modes. Only during the series of measurements does a change appear to take place that has an influence on permeation.

Due to the high contact pressures, it is expected that the membrane will begin to creep during operation and reduce its

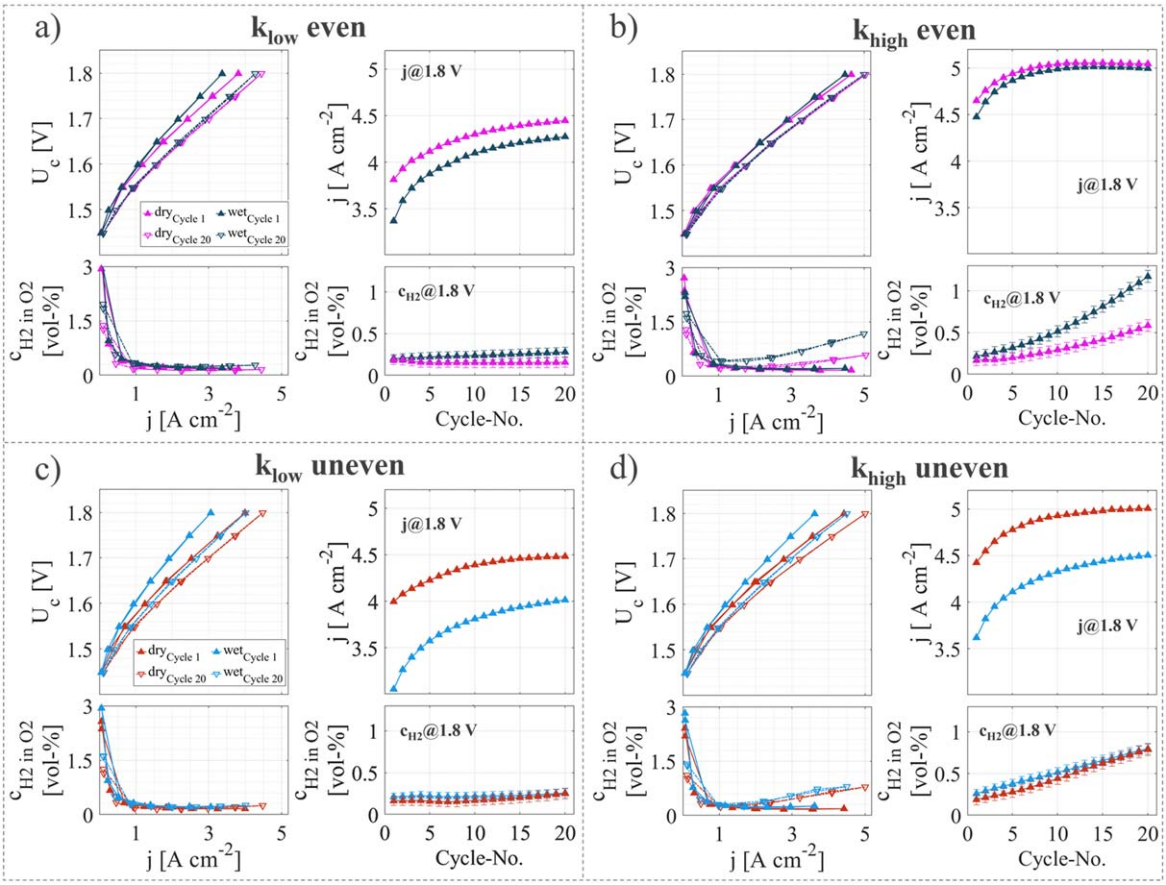

Figure 3. Polarization curves, H_2-in-O_2 concentrations on the anode side of 16 cm^2 PEM-WE single cells measured at 80 °C and ambient pressure are shown in the left graphs of each subfigure (a)–(d). On the right side of each partial figure, the relationship between the current density respectively the hydrogen permeation and the 20 measurement cycles at a cell voltage of 1.8 V is shown. Polarization diagrams: The solid lines with filled triangles pointing upwards represent the results of the first measurement cycle and the dashed lines with empty triangles pointing downwards show the last 20th measurement cycle. Magenta colors represent the results of the dry and evenly assembled test cells, light red colors represent dry but unevenly assembled test cells. The blue colors represent the wet-mounted CCMs. Light blue stands for uneven and dark blue for even contact pressure distribution. (a) shows the results for the low compression of the carbon PTL with balanced contact of the active area. (b) shows the same for the high compression. (c) and (d) show the results with uneven compression of the C-PTL over the active area for each compression rate. The cell voltage was increased to 1.8 V in 0.05 V increments, starting at 1.45 V and then reduced to 1.45 V in 0.1 V increments. The H_2-in-O_2 concentration measured in parallel is also displayed.

thickness, leading to increased local current density and permeation. To prove this assumption, the cross sections of the CCMs were analyzed after drying the samples in the cell. But, before removal, end-of-test (EOT) impedance measurements were taken at 1.45 V.

Impedance measurements.—The measured impedance data at 1.45 V are summarized in Fig. 4 for the different compression and assembly modes. Each mode "k_{low} even," "k_{high} even," "k_{low} uneven," and "k_{high} uneven" is presented separately in Figs. 4a –4d, comparing directly the begin-of test (BOT) and end-of-test (EOT) results of the wet and the dry mode.

Before starting the impedance measurement, the potential was adjusted and waited for 5 min at constant settings to ensure that the electrodes and PTLs were saturated with gas. During this waiting period, the cells that were assembled with the unevenly contacted CCM repeatedly experienced sudden increases and decreases in current. These jumps were repeated at intervals of approximately 40 to 60 s. At the beginning of the impedance measurement, the higher frequencies could be measured quickly without current jumps, but at lower frequencies, where the measurement time per frequency was significantly longer, the jumps were also measured. This is the reason for the larger scattering of the impedance values in Figs. 4c and 4d. It is assumed by the authors that the low contact pressure within the channels in case of Figs. 4c and 4d was the reason for the measured current jumps. If the contact pressure is too low, the gas bubbles, generated during the electrochemical reaction, most likely induce pressure drops which can influence the contact between the electrode and the PTL and therefore the current. It is expected that this influence will be greater at the beginning of the measurements because the mass transport of the gaseous and liquid phases through the PTLs is not yet in equilibrium.

The electrochemical interpretation of the presented spectra in Fig. 4 is also affected by the circumstances discussed regarding the polarization plots in Fig. 3. Since it is unclear how the expected current density distributions affect the shape of the semicircular structures of the spectra, a discussion of these data points is omitted here. Additionally, the influence of the described device-related errors in the high frequency range (left part of the 500 Hz label in Fig. 4) makes it a challenge to interpret the data measured in the higher frequency range. But, despite these difficulties, a shift of the impedance curves to higher real values in the impedance data correlates with higher contact resistances and higher effective membrane thicknesses. Therefore, the following discussion is limited to the differences in the shift of the spectra in the direction of the real axis.

Except for assembly mode "k_{high} even" (Fig. 4b), the inserted figures clearly show for the assemblies a shift of the spectra to lower real values when comparing the BOT with the EOT data. This shift is larger in case of the wet assembled CCMs in comparison to the dry assembled CCMs. An explanation for this observation could be

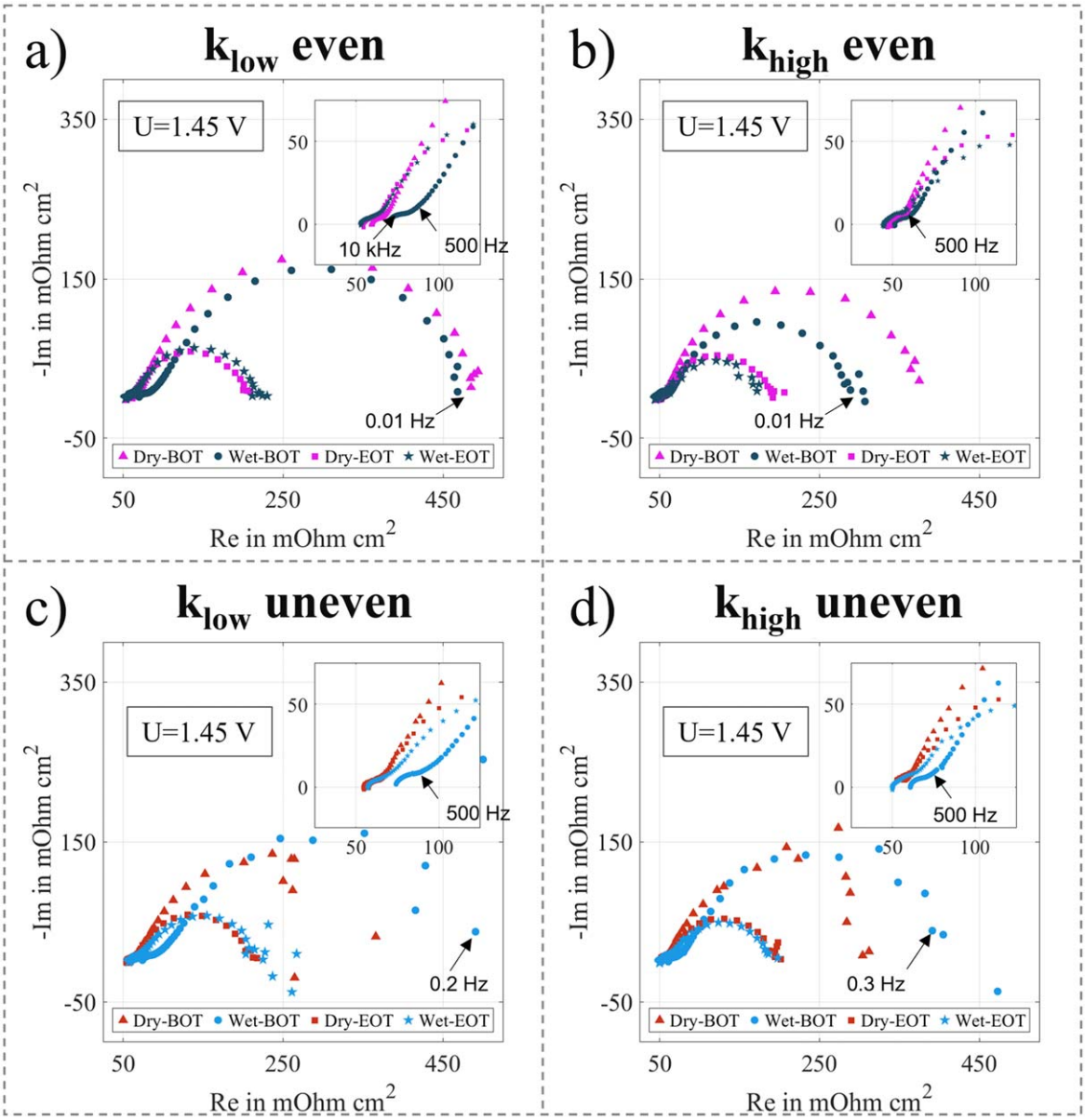

Figure 4. Exemplary Impedance spectra, measured at 1.45 V for the 4 cell assemblies, measured before (begin of test - BOT) the 20 polarization cycles and after (end of test - EOT) with a wet or dry assembled test cell. (a+b) show the measurement results of the even pressure distribution – (a) with low compression rate and (b) with high compression rate. The magenta-colored lines represent the dry assembled cells and the dark blue the wet assembled ones. Solid lines show the BOT measurement results, and the dashed lines show the EOT results of the even pressure distribution. (c+d) represent the impedance spectra of the cells assembled with the thin PTLs only. (c) shows the results for the low compression rate, (d) for the high compression rate. The red-colored lines represent the dry assembled cells and the light blue lines the wet assembled cells. The solid lines represent the BOT measurements, and the dashed lines represent EOT measurements.

the different swelling states of the membranes. Hoppe et al.[28] could show that the thickness increase by swelling of a dry Nafion™ 212 membrane, assembled between PTLs at 28 °C, can be larger than 10 μm, which is almost 30% of the total compression in the "k_{low}"-setup used in this study. In addition, the water uptake increases when the temperature increases, and the uptake can take several thousand seconds if the membrane is in direct contact with the water. Such an uptake process follows a typical course of a saturation process—fast at the beginning and slow at the end.[29] It is therefore very likely that the dry membrane thickness increases faster when in contact with water by swelling than the pre-swollen membrane, which takes longer but also increases in thickness in the end and thus achieves a comparable contact resistance. The described shift of the impedance curves, which disappeared towards the end of the measurement, is therefore interpreted as an indication that the swelling process which generates an additional pressure on the C-PTL is partly responsible for the formation of a lower contact resistance. In the case of "k_{high} even," with a higher compression factor of 42%, the additional swelling pressure has no influence, since the value is already significantly higher and the reduction in the resistance of the C-PTL becomes smaller and smaller the greater the contact pressure becomes.

In addition to the swelling of the membrane, the changing membrane thickness distribution, induced by the creeping membrane material, leads to a reduction in the effective membrane thickness and therefore the effective membrane resistance. Because of the wider thickness distribution under the ribs (Figs. 6a3 and 6b3 and 7a3 and 7b3), this effect is likely to be more pronounced in the 'k_{high}'-assemblies than in the "k_{low}"-assemblies. Both, the increased contact pressure and the reduced effective membrane resistance are

most likely the reason that the shift of the impedance values ends at higher values (over 50 mOhm cm^2) for "k_{low}" assembled cells (inserted figures in Figs. 4a and 4c) and lower values (below or at 50 mOhm cm^2) for "k_{high}" assembled cells (inserted figures in Figs. 4b and 4d).

Cross-sectional analysis.—As a reference for the following cross-sectional analysis, a pristine Nafion™ 212 membrane and a pristine Nafion™ 212-based CCM was first analyzed in its original state. During CCM assembly, the electrodes are hot-pressed onto the membrane. Since the electrodes have an irregularly rough surface, this structure is imprinted into the membrane, which leads to a broader thickness distribution of the membrane in comparison to its original state (Fig. 5). The extent of the electrode induced membrane thickness scattering can be determined by cross-sectional analysis of the pristine dry CCM and the pristine membrane. Since both references were also embedded in the resin, which can slightly dry out the sample upon contact, this interaction is included in the reference as with all samples, thus avoiding misinterpretations due to the effect of the resin on the samples. The thickness distribution of these references was used in the present study as a reference for all further samples in order to distinguish the changes that occurred in the test cell from those that were already present before the experiment.

The pristine Nafion™ 212 membrane was used as purchased for the embedding and cross-sectional analysis procedure and not further pretreated. Only the two protective films were removed right before embedding, as is also done before hot pressing. The reference CCM was prepared as described in the experimental section. By determining the membrane thickness over a sample length of slightly more than 12 mm, a representative frequency distribution of the thickness of a Nafion™ 212 membrane before and after hot pressing process could be created, which is shown in Fig. 5a).

The thickness distribution of the pristine dry membrane before hot pressing has a narrow distribution of 49 μm–52 μm, which is also reflected in a smaller scatter of the thickness over the sample length, see Fig. 5b). The thickness distribution of the pristine dry membrane after hot pressing, on the other hand, scatters significantly around the mean value of 50 μm, see Fig. 5b), which is also reflected in a wider frequency distribution width with values of 40 μm–55 μm. The maximum here is at 49 μm, which corresponds well with the maximum of the pristine membrane at 50 μm thickness. The distribution width of the hot-pressed membrane is caused by thickness variations of the electrodes, which penetrate the membrane unevenly during the hot-pressing process. Additionally, it should be emphasized that it cannot be ruled out that the resin material used for the preparation interacts with the ionomer material and may slightly distort the determination of the thickness distributions. But it can be assumed that this interaction, if it occurs, occurs equally in all samples. However, since this possibility of interaction cannot be excluded and it is also to be expected that the samples will exhibit additional irregularities over the sample length due to the flow field used, not only the thickness distributions but also the determined thicknesses as a function of sample length are presented to be able to assign the observed effects to the physical causes. Figures 5c and 5d show the merged cross section image of the reference-CCM and the reference-membrane, stretched in the direction of membrane thickness, since otherwise nothing would have been visible due to the ratio of thickness to length of about 1:270. The magenta contours show the edges detected during image analysis between the electrodes and the membrane as well as between the membrane and the resin.

After the EOT impedance- and short-circuit measurement, the thickness distribution of the membranes was determined for the different cell assembly modes according to the described method in the experimental section. Figure 6 summarizes the results for the low compression. For assembling "k_{low} even-wet," the stitched images are presented in the lower part of Fig. 6a1. The determined thickness as a function of sample length is presented in the upper part of Figs. 6a1. Figure 6a2 shows the same data in a histogram plot. As expected, the center value of the distribution is with 44 μm smaller than the value of the pristine membrane of the dry CCM, see Fig. 5a, because of the pre-swelling of the CCM.

The corresponding data for assembling "k_{low} uneven-wet" are represented in Fig. 6a3 to 6a5. While the scattering of the thickness values across the sample length in Fig. 6a1 is the same, the thickness values in Fig. 6a5 scatter in the rib regions stronger than in the channel regions, marked with the blue bars. This is because the flow field ribs press the 20 μm thick titanium fibers of the anode PTL through the catalyst layer into the membrane, leaving an imprint that remains even after drying and removal from the test cell. This can also be seen in the section of the original image in Fig. 6a7 in comparison to Fig. 6a6. There are semicircular depressions with a diameter of approximately 20 μm, which corresponds very well with

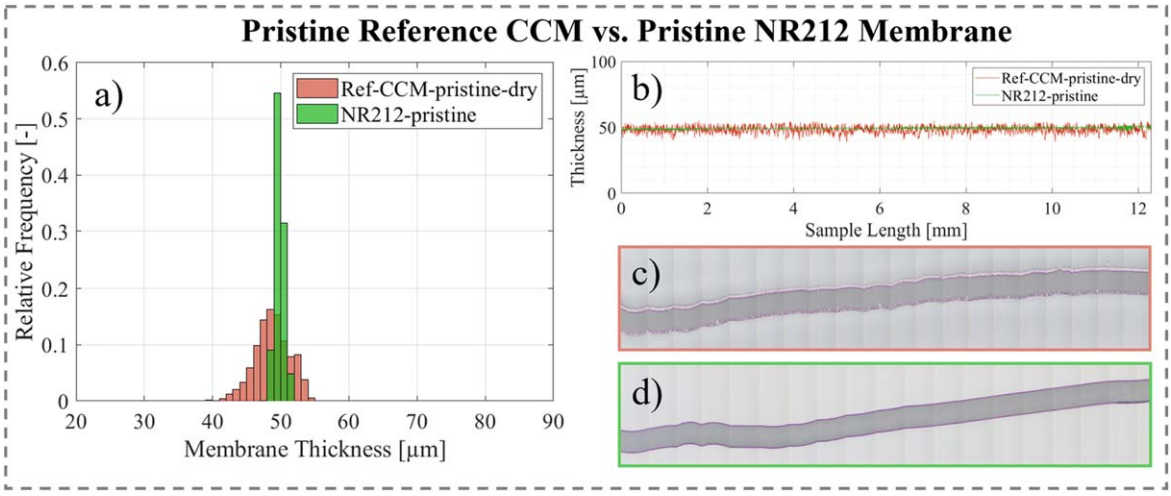

Figure 5. Comparison of the thickness distribution of a pristine dry Nafion™ 212 membrane and a pristine dry Nafion™ 212-based CCM in its original state. (a) Narrowband frequency distribution of the thickness of the Nafion™ 212 membrane (shown in green) with a maximum at approximately 50 μm and a slightly broader frequency distribution of the pristine CCM (shown in red) with a maximum at 49 μm. (b) The membrane thickness of the cross section of the pristine CCM (red line) and the pristine Nafion™ 212 membrane (green line) over the sample length. (c) shows the associated cross section of the pristine CCM stretched in the direction of the membrane thickness and (d) shows the associated cross section of the pristine Nafion™ 212 membrane stretched in the direction of membrane thickness.

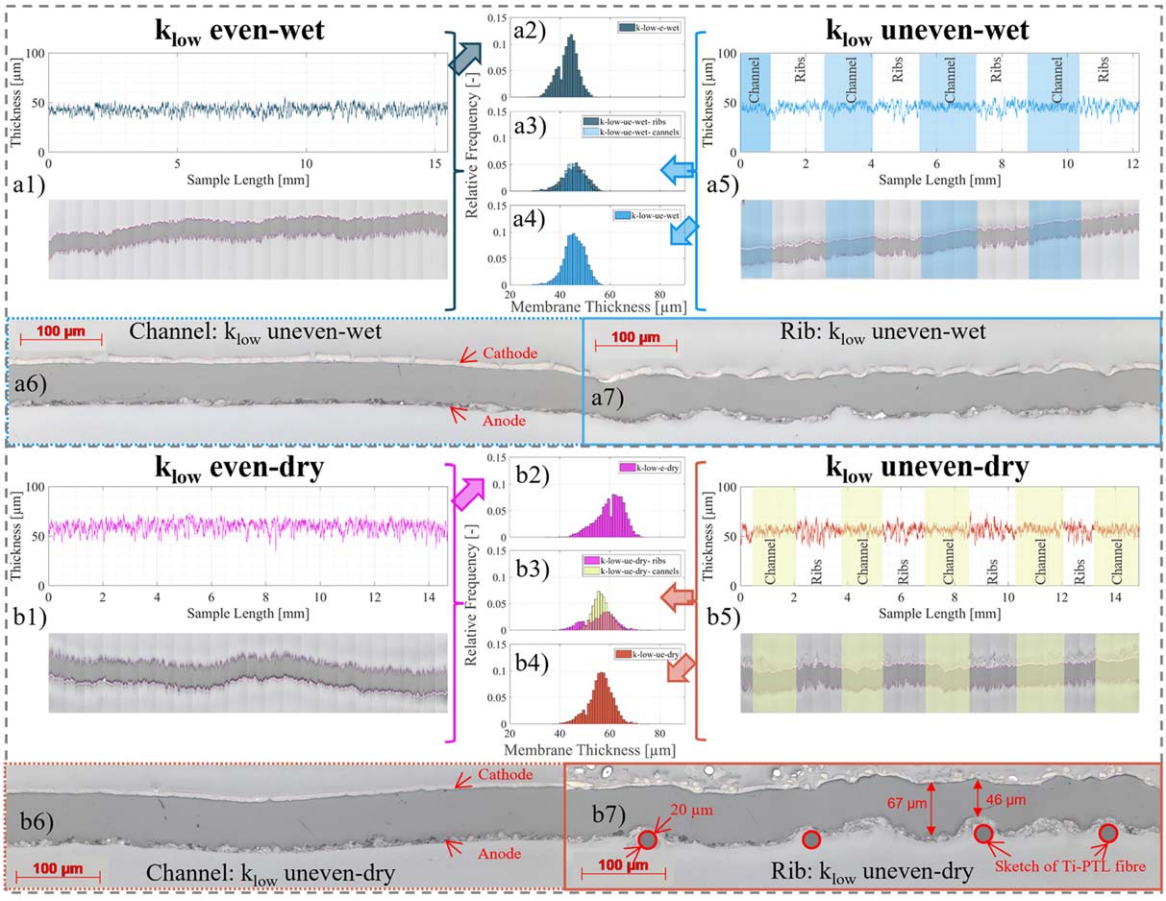

Figure 6. The post-mortem cross-sectional analysis of the measured CCMs: (a1) measured with a low compression rate of the C-PTL shows the membrane thickness of the cross section of the CCM over the sample length for "k_{low} even-wet" at the top, and the associated cross section in the lower section. A sectional profile can be seen, with the image stretched in the direction of the membrane thickness to clarify the sample cross section. (a2) shows the associated relative frequency distribution of the determined membrane thickness. (a5) shows the post-mortem cross-sectional analysis of the CCM for the cell configuration "k_{low} uneven-wet." The blue bars in (a5) indicate which parts of the sample were positioned in the areas of the channels of the flow field. A clear assignment is not possible due to the sample preparation proceeding and is not trivial due to the mirror-inverted overlap of the meander geometries in the cell (see Fig. 1d). (a3) shows the thickness distribution with a distinction between the areas positioned near to the ribs (dark blue bars) and near to the channels (light blue bars). The overall frequency distribution is presented in (a4). (a6) and (a7) show a part of a cross-sectional profile of the CCM under the channel region and respectively under the rib-region of the flow field in the original image scale of the uneven-setup. The corresponding representation can be found in (b1) and (b2) for "k_{low} even-dry" and (b5), (b4) and (b3) show the membrane thickness over the sample length, the frequency distribution divided into the areas of ribs (magenta-colored bars) and channels (yellow-colored bars) and the overall frequency distribution of the membrane thickness of "k_{low} uneven-dry." (b6) and (b7) show the original scale images of the CCM cross section under the channel region and respectively under the rib-region of the flow field in the uneven-setup. (b7) also shows sketched titanium fibers that press into the CCM, leaving an imprint.

the fiber diameters of the Ti-PTL used. These imprints cannot be seen in the areas of the CCM that were in contact with the PTL under the channels, see Fig. 6a6.

In other words, the membrane material has flowed away under the wires of the Ti-PTL. Such a creep process is not actually expected based on the macroscopic pressure values in Fig. 2. However, the thin wires concentrate the force flow, so the microscopic pressures will be much larger and may unexpectedly cause the membrane material to flow when the yield strength is exceeded. The flow of the material reduces the local force flow, which in turn leads to reduced material flow. Local flow thus reduces the local pressure. Therefore, the material can only flow in the local area between the titanium fibers, where sufficient space is available due to the material's porosity of 68%.

For this reason, material accumulation does not occur in the channel region, as no force-flow pressures above the yield strength can be generated there. These considerations lead to the assumption that the same membrane volume must always be present along the channel-rib areas. Unfortunately, the two-dimensional thickness distribution analyzes presented in this study do not provide direct information on three-dimensional volume conservation. However, in the supplementary material (Fig. S1), we derived an indirect pathway showing that the membrane volume assumes a constant value in the investigated areas for dry- and wet-installed CCMs, respectively. This means that it can be assumed that the membrane material only flows locally into and fills the pores.

Since the macroscopic pressure distribution in Fig. 2 for the "k_{low} even-wet" setup does not show the channel structure, the scatter of thickness values in Fig. 6a1 does not show the rib/channel structure and the magnitude of the scatter is closer to that of the ribs than to that of the channels in Fig. 6a5. However, this difference is more visible when comparing the "thickness as a function of sample length" plots. In the overall histogram plots, the difference is not so clear—the center of the thickness distribution and the widths of the distributions are comparable, see Figs. 6a2 and 6a4. The "uneven" configuration shows a greater proportion of thicker membrane regions and the "even" assembly mode shows a greater shift towards smaller membrane thicknesses. If the frequency distribution of the "uneven" configuration is decomposed into the channel and rib regions, it can be seen that the width of the thickness distribution under the ribs is equal to the distribution width of the "even" assembly mode, see Fig. 6a3.

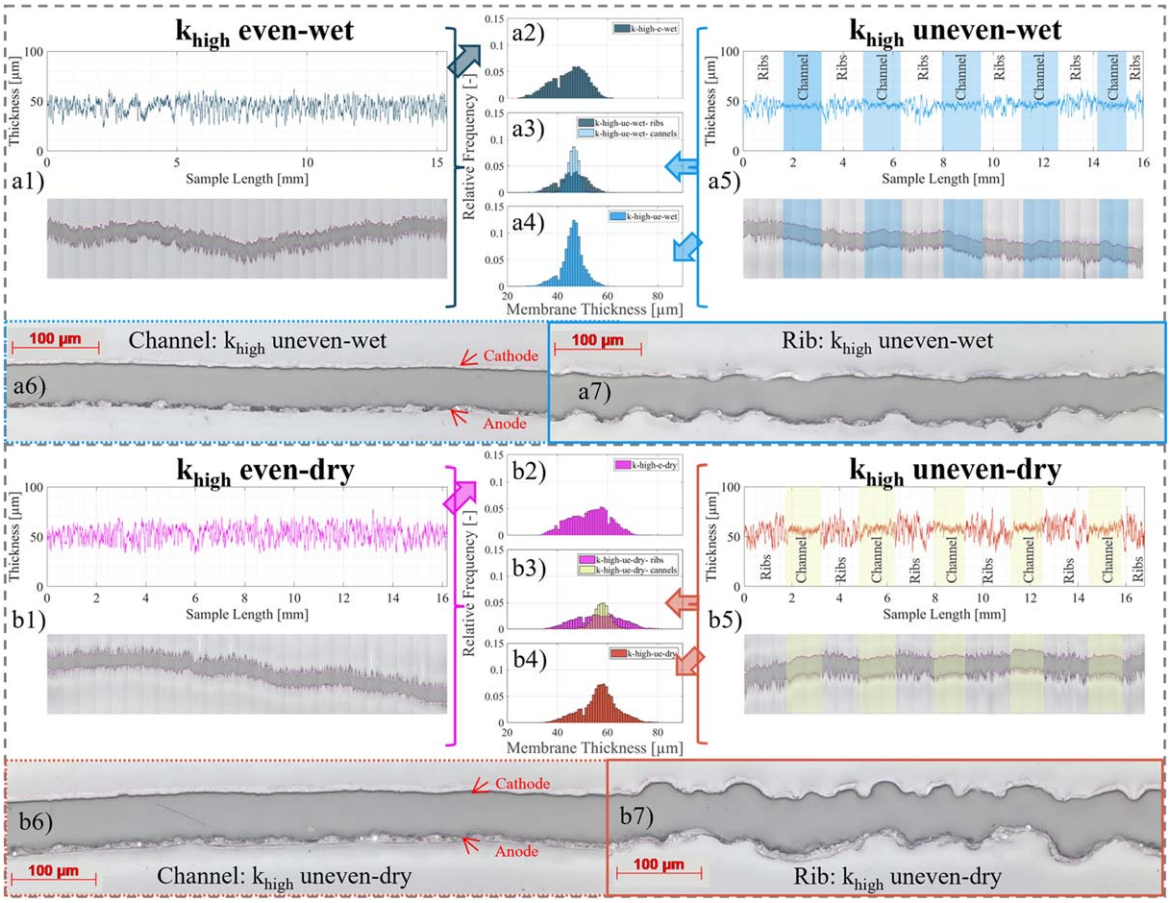

Figure 7. The post-mortem cross-sectional analysis of the measured CCMs with high compression rate: (a1) shows the membrane thickness of the cross section of the CCM over the sample length for "k_{high} even-wet" at the top, and the associated cross section in the lower section. A sectional profile can be seen, with the image stretched in the direction of the membrane thickness to clarify the sample cross section. A small original section is included below to visualize the real thickness to length ratio. (a2) shows the associated relative frequency distribution of the determined membrane thickness. (a5) shows the same for the cell configuration "k_{high} uneven-wet." The blue bars indicate which parts of the sample were positioned in the areas of the channels of the flow field. A clear assignment is not possible due to the sample preparation and is not trivial due to the mirror-inverted overlap of the meander geometries (see Fig. 1d). (a3) shows the thickness distribution with a distinction between the areas positioned near to the ribs (dark blue colored) and near the channels (light blue colored). The overall frequency distribution is shown in (a4). (a6) and (a7) show a part of a cross-sectional profile of the CCM under the channel region and respectively under the rib-region of the flow field in the original scale of the uneven-setup. The corresponding representation can be found in (b1) and (b2) for "k_{high} even-dry" and (b5) shows the membrane thickness over the sample length, (b4) summarizes the frequency distribution divided into the membrane thicknesses in the areas of the ribs (magenta-colored bars) and the channels (yellow-colored bars) and overall the frequency distribution of the membrane thickness of "k_{high} uneven-dry" is shown in (b4). (b6) and (b7) show a part of a cross-sectional profile of the CCM under the channel region and respectively under the rib-region of the flow field in the original scale of the "k_{high} uneven-dry" configuration.

The "k_{low} even/uneven-dry" assemblies, represented in the bottom row of Fig. 6, show a similar situation, but the centers of the thickness distributions are higher than in the wet assemblies. The reason for this is that the wet samples were able to expand in all directions before cell assembly. However, when drying in the cell, the tangential movement is disturbed by the fixation so that the material can only flow in the direction of the membrane surface normal. Material that previously moved sideways can no longer move back during drying and is missing - the resulting reduced thickness was retained during disassembly. The dry sample, on the other hand, was fixed in the cell and swelled when in contact with water, expanded (this creates the higher contact pressure compared to the wet sample) and contracted again when the CCM is dried in the test cell.

The center of the thickness frequency distribution for the "k_{low} even-dry" arrangement is slightly higher than the center of the "k_{low} uneven-dry" assembling. The reason for this is currently unknown to the authors. More important for this study is the larger width of the thickness distribution, which indicates a stronger membrane creep due to the additional contact pressure from the swelling process in the test cell. As already shown for "k_{low} wet," the splitting of the frequency distribution of the membrane thickness in the uneven assembling into rib and channel regions shows a clear difference in the distribution width and here too, a clear agreement between the distribution width of the rib-region in the "uneven" mode with the distribution width of the "even" assembly mode can clearly be seen (compare Figs. 6b3 and 6b2). The difference in membrane thickness between the CCM areas located near to the ribs or close to the channels of the flow fields can be more clearly distinguished in the dry installation mode than in the wet installation method, where the membrane creep is less due to pre-swelling.

The "k_{high} even/uneven-wet" arrangement exerts an even higher pressure on the membrane. The resulting thickness distributions are shown in Figs. 7a2 and 7a4. It is clearly visible that the higher contact pressure increases the scatter in the thickness distribution under the ribs of the "k_{high} uneven-wet" arrangement, which is reflected in a wider distribution of thickness values in Fig. 7a4. The comparison of the scatter of the thickness values over the sample length again shows a clear improvement in the distinguishability of the thicknesses, influenced by the position near to the rib/channel areas, marked with the blue bars in Fig. 7a5. The marking does not explicitly mean that the sample was definitely located at this point in

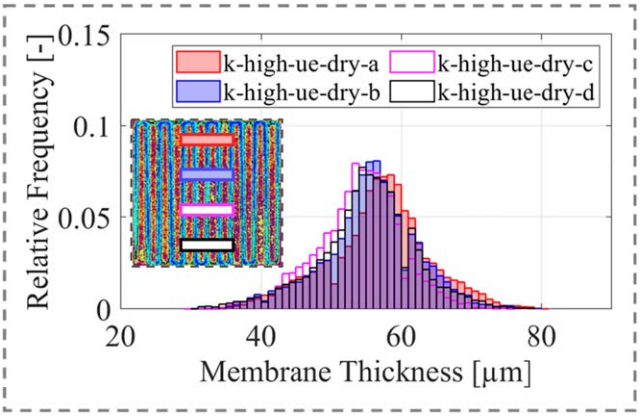

Figure 8. The relative frequency distribution of the measured membrane thickness across the sample length of four different sample cross sections of one CCM. The sample position is shown in the inserted contact pressure distribution figure. The direction of the sample cross section is identical for all four samples to demonstrate the representativeness of the thickness distributions.

the flow field geometry. Due to the sample preparation, where the CCM is cut into pieces after disassembling the cell and the sample is then embedded, cured, sectioned and polished, it can only be indicated—however, the areas were subject to the influence of the higher contact pressures caused by the ribs, which resulted in a stronger flow of the membrane material. This should be emphasized at this point. The division of the frequency distribution here also shows a correspondence in the broader distribution of the rib-region, comparable to the „even‘ assembled CCM, see Fig. 7a3. Whether a cross section with the corresponding orientation perpendicular to the ribs and channels is representative of a sample or not was investigated by analyzing one CCM at four different locations. The resulting frequency distributions of the thicknesses are shown in Fig. 8, including the marking of the corresponding sampling position. These data show that the frequency distributions are comparable within a range of ±4 µm—one thickness distribution is therefore representative for the others.

It is noticeable that the thickness distribution is more asymmetric in the "k_{high} even-wet" arrangement compared to the overall "k_{high} uneven-wet" arrangement. Additionally, the smallest values are below 30 µm while the largest values are up to 60 µm. Compared to the thickness of membrane in a pristine CCM, see Fig. 5a, the thickness range is doubled to a range of 30 µm–60 µm due to the higher compression and the wet state of the CCM.

This is comparable to the arrangement "k_{high} even-dry," see Fig. 7b2, where the membrane thickness is in the range of 35 µm–70 µm. For the "k_{high} uneven-dry" arrangement, based on the pressure distribution in Fig. 2, it is to be expected that the larger thickness distribution is limited to the rib areas of the flow field. The measurement data in Fig. 7b3–7b5 show exactly this scattering pattern. Since the creep effects are limited to the rib areas, the thickness distribution is still symmetrical, but also greatly broadened, even more than the "k_{high} even-dry" configuration. Divided into the distribution widths of rib/channel influenced areas (yellow bars in Fig. 7b5) indicating the channel regions), one can also see the clear influence of the higher contact pressures on the membrane flow under the flow field ribs (see Fig. 7b3).

The original scaled images in Figs. 7a6 and 7a7 of the "k_{high} uneven-wet" cell assembly mode and in Figs. 7b6 and 7b7 of the "k_{high} uneven-dry" arrangement show once again the large difference in deformation due to the different contact pressures.

The membrane creep is so large in the different cell arrangements "k_{high} even/uneven-wet/dry" that the question arises as to where the current flows through these inhomogeneous membrane thicknesses. A homogeneous current density distribution is unlikely with such broad membrane thickness distribution. The regions with lower membrane thickness (for example in Fig. 6b7) – 67 µm thickness vs 46 µm thickness) are accompanied with lower ohmic resistances which results in higher local current densities when a constant voltage is applied. Based on the example in Fig. 6b7 the local current will be significantly higher at the thinner spots (67 µm/46 µm = 1.46 – up to 46%). Especially in technical cells, where the cost factor for the selected PTLs is an important selection criterion, and where the use of thin membranes is becoming increasingly important to meet the efficiency requirements, special attention to the PTL/catalyst layer contact is very important. Recent studies also show that increasing current density can also increase aging effects such as iridium dissolution.[30]

Together with the fact that hydrogen permeation trough the membrane increases with increasing current density,[10,16,31–34] this observation provides a first hint of an explanation for the increase of hydrogen in oxygen concentration in Fig. 3b. Of all the cell arrangements investigated, "k_{high} even-wet/dry" generates the strongest creep of membrane material, resulting in increasingly thinner membrane regions from cycle to cycle. These thinner membrane regions can lead to a change in the local current density, which in turn leads to higher local hydrogen permeations. In case of the wet assembling, the membrane is thinner than in the case of the dry assembling. Together with a higher compression of the C-PTL, this generates membrane areas with thicknesses of less than 30 µm (Fig. 7a2). This is the lowest thickness observed for all assemblies, which could explain the highest value for the measured hydrogen permeation for the "k_{high} even-wet" assembly mode, see Fig. 3b. The situation is similar to "k_{high} even-dry," but here the membrane is thicker overall. For the cell arrangement of "k_{high} uneven-wet/dry" Fig. 2d shows that large areas are free of high contact pressures. Therefore, the membrane creep occurs only under the ribs which reduces the impact on the hydrogen permeation (Fig. 3d) and can be seen in the representation of the membrane thickness as a function of sample length in Fig. 7b5.

In case of "k_{low} uneven-wet/dry," no increase in hydrogen permeation can be measured within the measurement uncertainty. Only for assembling "k_{low} even-wet" a small increase of hydrogen permeation is visible from cycle to cycle. This could be related to the lower membrane thickness due to the pre-swelling, but the difference of the measurement values of "dry" and "wet" assembling is too small compared to the measurement uncertainty, see Fig. 3a, to make a clear statement here.

The measured data on hydrogen permeation and change in membrane thickness distribution suggests that there is a relationship, but it is very likely that the cause-effect relationship is due to a change in the current density distribution during operation caused by membrane creep. This most likely affects the change in the measured hydrogen permeation.

The important question arises whether the creep of the membrane material is caused by the local pressure under operating conditions or by the temperature increase in the membrane caused by the electrochemical reaction. To answer this question, additional CCMs were installed with the cell configuration "k_{high} uneven-wet" and "k_{high} uneven-dry." The cells were then operated in the same way as the previously examined CCMs, but without any electrochemical reaction. The results of the membrane thickness distribution after drying and cell disassembly are compared in Figs. 9a1 und 9b1 with the results shown in Figs. 7a4 and 7b4.

With a slight difference in the center of the thickness distributions for the wet installation, but with impressive agreement with the dry installation, the thickness data results show that the observed membrane creep appears to be independent of the electrochemical reaction. This is also summarized in Figs. 9a2, 9a3, 9b2 and 9b3, where it clearly can be seen that it has an influence on whether the membrane is exposed to the high contact pressure under the ribs. Therefore, it is very likely that membrane creep is only induced by the chosen contact pressure in combination with the PTL, which transfers the applied contact pressure, depending on its structure, to higher local pressure values.

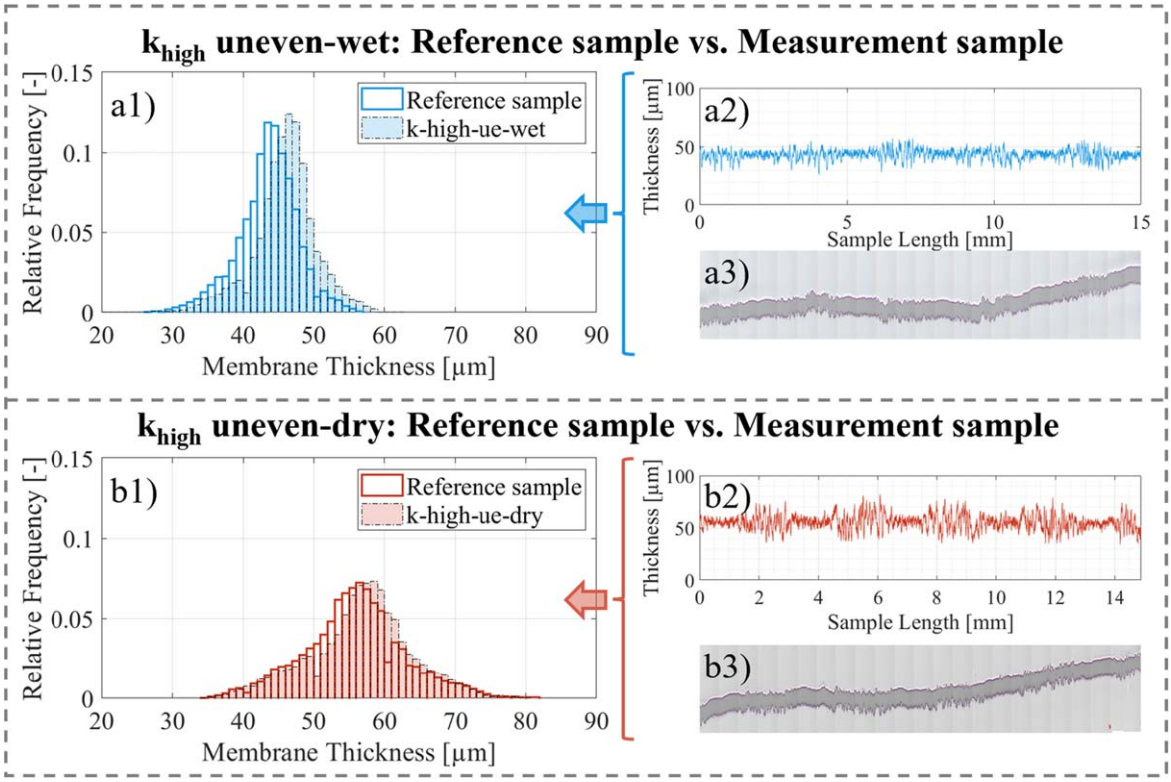

Figure 9. The post-mortem cross-sectional analysis of the measured CCMs compared to the reference samples stayed in the cell over the same period of time at cell temperature and flow rate. The cell mode was chosen with non-uniform contact pressure distribution at high compression. (a1) Thickness distribution for the dry-mounted CCMs, (a2) represents the thickness as a function of sample length and (a3) shows the accompanying cross-sectional profile stretched in the direction of membrane thickness. (b1)–(b3) shows it accordingly for the wet-mounted reference sample.

Conclusions

Published results on hydrogen permeation in PEM water electrolysis combined with publications on the creep behavior of Nafion™ membranes suggest that membrane material can also creep during PEM electrolysis operation due to the contact pressures used, which can result in increased hydrogen permeation.

In this study, the influence of different compression values, even or uneven contact pressure distribution of a dry or wet assembled PEM water electrolysis CCM was investigated through electrochemical polarization and hydrogen crossover measurements as well as cross-sectional analyzes. The contact pressure distribution was examined in advance with pressure sensitive foils and post-mortem analyzes of the CCMs were carried out in cross-sectional analyzes to examine the membrane thickness distribution after the same operating time of 75 h.

By repeating the polarization measurements 20 times, the investigations reveal that the measured values in current density follow a saturation behaviour. The values approach limit values, so that the CCMs only deliver reproducible measured values after a few cycles. Depending on the test cell assembling, some values, such as hydrogen permeation, do not converge at all. Post-mortem cross-sectional analyzes of the CCMs after drying and removal from the cell showed clearly a visible creep in the membrane material, especially under the ribs of the flow fields used. The spread of the thickness distribution is larger at high compression values of the PTL and larger with dry-installed CCMs. A membrane that was originally 49 µm thick can be locally reduced to values below 30 µm and locally increased to up to 70 µm. The creep of membrane material generally depends on the contact pressure and operation conditions used. However, in the present study it was shown that the electrochemical reaction has no influence on the observed membrane creep. Furthermore, the different cell arrangements show that the observed hydrogen permeation can be correlated with the different membrane thickness distributions, which were significantly broadened by the creeping membrane material.

However, according to the authors, it is unlikely that the increasing hydrogen permeation is directly induced by the thickness change. It is more likely that the change in the membrane thickness causes a change in the local current density and that the regions with higher current densities are responsible for the higher hydrogen permeation. However, the local current density is a function of local contact resistance, local membrane thickness, electrochemistry and other aspects. In the future, further studies are needed to clarify the dependencies between the change in membrane thickness due to membrane creep, the change in the local current density, and in hydrogen permeation.

ORCID

A. Hintzen https://orcid.org/0000-0002-4058-6056
M. Stähler https://orcid.org/0000-0003-4051-9950

References

1. F. Barbir, "PEM electrolysis for production of hydrogen from renewable energy sources." *Sol. Energy*, **78**, 661 (2005).
2. M. Carmo, "A comprehensive review on PEM water electrolysis." *Int. J. Hydrogen Energy*, **38**, 4901 (2013).
3. J. Chi, "Water electrolysis based on renewable energy for hydrogen production." *Chin. J. Catal.*, **39**, 390 (2018).
4. R. Harvey, R. Abouatallah, and J. Cargnelli, *PEM Electrolysis for Hydrogen Production* (CRC Press, Boca Raton, FL)315 (2016).
5. U. Babic, M. Suermann, F. N. Buehi, L. Gubler, and T. J. Schmidt, "Review-identifying critical gaps for polymer electrolyte water electrolysis development." *J. Electrochem. Soc.*, **164**, F387 (2017).
6. S. A. Grigoriev, P. Millet, S. V. Korobtsev, V. I. Porembskiy, M. Pepic, C. Etievant, C. Puyenchet, and V. N. Fateev, "Hydrogen safety aspects related to high-pressure polymer electrolyte membrane water electrolysis." *Int. J. Hydrogen Energy*, **34**, 5986 (2009).
7. F. Scheepers, M. Stähler, A. Stähler, E. Rauls, M. Müller, M. Carmo, and W. Lehnert, "Improving the efficiency of PEM electrolyzers through membrane-specific pressure optimization." *Energies*, **13**, 612 (2020).

8. S. A. Grigoriev, V. I. Porembskiy, S. V. Korobtsev, V. N. Fateev, F. Aupretre, and P. Millet, "High-pressure PEM water electrolysis and corresponding safety issues." *Int. J. Hydrogen Energy*, **36**, 2721 (2011).
9. H. Janssen, "Safety-related studies on hydrogen production in high-pressure electrolysers." *Int. J. Hydrogen Energy*, **29**, 759 (2004).
10. M. Stähler, A. Stähler, F. Scheepers, M. Carmo, W. Lehnert, and D. Stolten, "Impact of porous transport layer compression on hydrogen permeation in PEM water electrolysis." *Int. J. Hydrogen Energy*, **45**, 4008 (2020).
11. K. Ayers, N. Danilovic, R. Ouimet, M. Carmo, B. Pivovar, and M. Bornstein, "Perspectives on low-temperature electrolysis and potential for renewable hydrogen at scale." *Annual Review of Chemical and Biomolecular Engineering*, **10**, 219 (2019).
12. W. R. Chang, J. J. Hwang, , and S. H. Chan, "Effect of clamping pressure on the performance of a PEM fuel cell." *J. Power Sources*, **166**, 149 (2007).
13. M. Espinoza, M. Andersson, J. Yuan, and B. Sundén, "Compress effects on porosity, gas-phase tortuosity, and gas permeability in a simulated PEM gas diffusion layer." *Int. J. Energy Res.*, **39**, 1528 (2015).
14. S. H. Frensch, A. C. Olesen, S. S. Araya, and S. K. Kær, "Model-supported characterization of a PEM water electrolysis cell for the effect of compression." *Electrochim. Acta*, **263**, 228 (2018).
15. R. Omrani and B. Shabani, "Hydrogen crossover in proton exchange membrane electrolysers: the effect of current density, pressure, temperature, and compression." *Electrochim. Acta*, **377** (2021).
16. A. Martin, P. Trinke, B. Bensmann, M. Stähler, A. Stähler, F. Scheepers, M. Carmo, and W. Lehnert, "The effect of cell compression and cathode pressure on hydrogen crossover in PEM water electrolysis." *J. Electrochem. Soc.*, **169** (2022).
17. M. Al-Baghdadi, "Mechanical behaviour of PEM fuel cell catalyst layers during regular cell operation." *International Journal of Energy and Environment*, **1**, 927 (2010).
18. S. H. Frensch, F. Fouda-Onana, G. Serre, D. Thoby, S. S. Araya, and S. K. Kær, "Influence of the operation mode on PEM water electrolysis degradation." *Int. J. Hydrogen Energy*, **44**, 29889 (2019).
19. S. A. Grigoriev, K. A. Dzhus, D. G. Bessarabov, and P. Millet, "Failure of PEM water electrolysis cells: case study involving anode dissolution and membrane thinning." *Int. J. Hydrogen Energy*, **39**, 20440 (2014).
20. P. Lettenmeier et al., "Durable membrane electrode assemblies for proton exchange membrane electrolyzer systems operating at high current densities." *Electrochim. Acta*, **210**, 502 (2016).
21. U. Babic, M. Tarik, T. J. Schmidt, and L. Gubler, "Understanding the effects of material properties and operating conditions on component aging in polymer electrolyte water electrolyzers." *Journal of Power Source*, **451**, 227778 (2020).
22. S. Garbe, J. Futter, A. Agarwal, M. Tarik, A. A. Mularczyk, T. J. Schmidt, and L. Gubler, "Understanding degradation effects of elevated temperature operating conditions in polymer electrolyte water electrolyzers." *J. Electrochem. Soc.*, **168**, 044515 (2021).
23. A. Stähler, M. Stähler, F. Scheepers, M. Carmo, and D. Stolten, "Reusability of decal substrates for the fabrication of catalyst coated membranes." *Int. J. Adhes. Adhes.*, **98** (2020).
24. M. Stähler, "A completely slot die coated membrane electrode assembly." *Int. J. Hydrogen Energy*, **44**, 7053 (2019).
25. C. Liu, M. Carmo, G. Bender, A. Everwand, T. Lickert, J. L. Young, T. Smolinka, D. Stolten, and W. Lehnert, "Performance enhancement of PEM electrolyzers through iridium-coated titanium porous transport layers." *Electrochem. Commun.*, **97**, 96 (2018).
26. A. Stähler, M. Stähler, F. Scheepers, W. Lehnert, and M. Carmo, "Scalable implementation of recombination catalyst layers to mitigate gas crossover in PEM water electrolyzers." *J. Electrochem. Soc.*, **169**, 1 (2022).
27. M. Stähler, A. Burdzik, I. Friedrich, A. Everwand, and F. Scheepers, "Oxygen flow rate measurement as a whistleblower for degradation effects in PEM water electrolysis." *Int. J. Hydrogen Energy*, **78**, 682 (2024).
28. E. Hoppe, S. Holtwerth, M. Müller, and W. Lehnert, "An ex situ investigation of the effect of clamping pressure on the membrane swelling of a polymer electrolyte water electrolyzer using X-ray tomography." *J. Power Sources*, **578**, 233242 (2023).
29. P. W. Majsztrik, M. B. Satterfield, A. B. Bocarsly, and J. B. Benziger, "Water sorption, desorption and transport in Nafion membranes." *J. Membr. Sci.*, **301**, 93 (2007).
30. A. P. Dam, T. Franz, G. Papakonstantinou, and K. Sundmacher, "Catalyst dissolution in PEM water electrolysis: Influence of time, current density and Iridium ion transport in single-pass and recirculation water flow modes." *Applied Catalysis B: Environment and Energy*, **365**, 124946 (2025).
31. P. Trinke, "Current density effect on hydrogen permeation in PEM water electrolyzers." *Int. J. Hydrogen Energy*, **42**, 14355 (2017).
32. M. Bernt, J. Schröter, M. Möckl, and H. A. Gasteiger, "Analysis of gas permeation phenomena in a PEM water electrolyzer operated at high pressure and high current density." *J. Electrochem. Soc.*, **167**, 124502 (2020).
33. A. Martin, P. Trinke, B. Bensmann, and R. Hanke-Rauschenbach, "Hydrogen crossover in PEM water electrolysis at current densities up to 10 A cm^{-2}." *J. Electrochem. Soc.*, **169**, 094507 (2022).
34. S. Fahr, F. K. Engel, S. Rehfeldt, A. Peschel, and H. Klein, "Overview and evaluation of crossover phenomena and mitigation measures in proton exchange membrane (PEM) electrolysis." *Int. J. Hydrogen Energy*, **68**, 705 (2024).